The Relation between Ejection Mechanism and Ion Abundance in the Electric Double Layer of Drops

Victor Kwan,[†] Ryan O'Dwyer,[†] David Laur,[†] Jiahua Tan,[†,‡] and Styliani Consta[*,†]

†*Department of Chemistry, The University of Western Ontario, London, Ontario, Canada N6A 5B7*

‡*College of Chemistry, Nankai University, Tianjin, P. R. China 300071*

E-mail: sconstas@uwo.ca

Abstract

The composition of outer drop layers has been associated with distinct chemical reactivity. We use atomistic modeling to examine how the composition of the surface excess charge layer (SECL) is related to the ejection mechanisms of ions. Even though the drop disintegration is inherently a non-equilibrium process we find that the equilibrium ion distribution in SECL predicts the ions that are ejected. The escape of the ions in aqueous drops takes place from conical protrusions that are global drop deformations and their appearance is independent of the location of a single ion. Our results agree with the equilibrium partition model, which associates the mass spectrum with the distribution of analytes in the drop's double electric layer. We present evidence that atomistic simulations of minute nano-drops cannot distinguish Rayleigh fission from the ion evaporation mechanism.

Introduction

Highly charged drops are a key constituent of thunderclouds[1] and man-made aerosols, the applications of which include ink-jet printing,[2] mass spectrometry ionization methods,[12–20] and the emerging area of micro-reactors.[3–10]

However, knowledge of the charge transfer mechanisms in the distinct micro (nano)-drop environment is still limited.[11]

In the context of aerosol-based ionization methods in mass spectrometry it has often been suggested that the drop chemistry determines the final charge state of the macroions reported in the spectrum.[21–23]

In previous research we have investigated the drop composition and electric properties using atomistic modeling.[24–27] In this article, we relate the equilibrium drop structure to the preferential ion ejection when mixture of ions are present. Additionally, it is shown that direct molecular dynamics simulations of minute nanodrops do not provide sufficient evidence for the validity of the ion-evaporation mechanism.[28–30]

The relation of the structure of a charged drop with the ion ejection has been a central question over several decades in mass spectrometry and atmospheric chemistry. The equilibrium partition model (EPM) of C. Enke hypothesizes two regions in a drop, a core region, and an outer region that carries the surface charge.[31,32] The model infers by comparisons with experiments that the species seen in the mass spectrum are those that make up the surface charge. Since EPM is a macroscopic qualitative model, it cannot directly provide the thickness and composition of the surface excess charge layer (SECL)

as well as it cannot test the hypothesis that the composition of SECL determines the mass spectrum. Surprisingly, it is only recently that the structure of a highly charged nanodrop was analyzed by using atomistic simulations.[25–27] In earlier studies the continuum modeling of the charge distribution in non-evaporating drops that was performed by our group[33] and recently by the Zare group[34] are in excellent agreement.

In the studies, we consider drops that contain several single ions. The maximum amount of charge a drop can hold just before spontaneous fragmentation is estimated by the Rayleigh limit.[35–39] We define this limit by using the Rayleigh fissility parameter (X) given as

$$X = \frac{Q^2}{64\pi^2\gamma\varepsilon_0 R^3} \approx \left(\frac{Q}{Q_\mathrm{r}}\right)^2 \qquad (1)$$

where Q is the drop charge, γ the surface tension, ε_0 and R are the permittivity of vacuum and the radius of the drop, respectively. When $X = 1$ the system is at the Rayleigh limit. The drop radius at the Rayleigh limit will be denoted as R_r and the corresponding charge Q_r. Therefore, X can also be expressed by the second equality in Eq. 1. At $X < 1$ the drop is said to be "below the Rayleigh limit". Under these conditions the drop is in a metastable state the lifetime of which is determined by the degree of deviation from the Rayleigh limit. An uneven breaking of a drop is energetically favorable. At $X > 1$ the drop is said to be "above the Rayleigh limit"

Here we summarize the general features of the structure of a charged drop. In the charged drops, we have identified the surface excess charge layer (SECL) and the maximum ion concentration region (MICR). The trend that we have found in previous studies[26,27] of drops of different sizes and ions indicates that the presence of SECL with thickness 1.5 nm-2.0 nm is a robust feature that spans the entire range of drop sizes including the micro-drops. Simulations of drop sizes with a diameter $<$ 16 nm with Na^+ or Cl^- ions have shown that 55%-24% (from a larger to a smaller drop) of the ions reside in SECL. The charge distribution in SECL is the sum of the ion charge (free charge) and the solvent polarization. The larger the drop, the smaller the effect of the ions in the solvent polarization.

Toward the interior, the ion distribution is expected to show an exponential decay as it is predicted by the solution of the non-linear Poisson-Boltzmann equation (NPB) for a rigid spherical drop.[25,26,33] The characteristic decay length[25,26,33] is expressed as

$$\lambda_\mathrm{PB} \approx \frac{\epsilon k_\mathrm{B} T}{\sigma} \qquad (2)$$

where k_B is Boltzmann constant, T is temperature, ϵ is the permittivity of water and $\sigma = \frac{|Z|e^2}{4\pi R_\mathrm{e}^2}$ for ions of charge $\pm 1e$, where e is the charge of the electron, $|Z|$ is the absolute value of drop charge in units of e. Here the assumption is that there are no counterions. For the drop comprised 3×10^4 H_2O molecules and 44 Na^+ ions (radius equal to 6.08 nm) $\lambda_\mathrm{PB} = 1.08$ nm if we consider a dielectric constant (experimental) $\varepsilon \approx 61.7$ at $T = 350$ K.

We have identified MICR as the region in the ion radial distribution that is delimited by a straight line parallel to the x-axis that starts from the ion distribution point with abscissa $r_\mathrm{max} - \lambda_\mathrm{PB}$ (where r_max is the distance where the maximum ion concentration is found) and intersects outward the ion distribution. The larger the drop, the larger the λ_PB value (because the surface charge density decreases), the slower the decay of the charge distribution. The maximum of the ion concentration decreases with size. The presence of counterions increases the concentration of the excess ions on the drop outer layers.[26] As the size of the drops decreases, SECL becomes comparable in size to MICR. In drops composed of $\approx$ 1000 H_2O molecules (radius $\approx$ 2 nm) λ_PB is comparable to the drop radius, and for this reason the radial ion distribution is nearly uniform.

A drop disintegrates via solvent evaporation and ion ejection. Ion ejection may take place either via a Rayleigh mechanism[35] or ion evaporation.[28,29] The Rayleigh mechanism involves release of substantial amount of charge from jets formed on the drop. IEM has been defined as the release of a single solvated ion

from the parent drop before the Rayleigh limit is reached. Macroscopic models of the ion evaporation mechanism have been developed by Iribarne-Thomson[28,29] and Fenn-de la Mora-Labowsky.[30,40] Hereafter, the latter model will be referred as Labowsky et al.. Both models consider a charged spherical drop at equilibrium and they treat the release of a single ion by first order kinetics. It has been supported experimentally that IEM occurs before Rayleigh fission in drops with a radius of approximately 10 nm. The models do not account for the drop structure and the ion spatial distribution. In the kinetic equation the total concentration of the ions in the drop is considered. Details about the effect of the charge sign on the drop size at which IEM dominates are presented in the study of Iribarne and Thomson.[28]

Models and Simulation Methods

Equilibrium simulations of drops

We performed molecular dynamics (MD) simulations of charged drops comprised (a) water and Na^+, Cs^+, Li^+ and protonated histidine (His^+) ions and (b) solvents with a dielectric constant less than that of water and Na^+ ions. Details of the systems are presented in Table 1. The simulations were performed by using the software NAMD version 2.12.[41] Newton's equation of motion for each atomic site was integrated using the velocity-Verlet algorithm with a time step of 1.0 fs. The trajectories were analyzed using VMD 1.9.2.[42] The production runs are for 40 ns for each system.

The water molecules were modeled with the TIP3P (transferable intermolecular potential with 3 points)[43] -CHARMM and the TIP4P/2005[44] and the ions with the CHARMM36m[45,46] and OPLS (Optimized Potentials for Liquid Simulations),[47,48] respectively. The TIP3P-CHARMM is a m(odified)TIP3P, which is the original TIP3P with Lennard-Jones potential on the hydrogen sites. Hereafter, we will use the notation TIP3P for this water model. In the water-histidine

systems the charge carriers are single protonated L-histidine mono-peptides, where the N-terminus is acetylated and the C-terminus is capped by N-methylamide. In this work, we define the position 2 carbon on the imidazole ring as the location of the positive charge as it is approximately the center of the resonance structure.

The structure of sodiated drops comprised acetonitrile (ACN), methanol (MeOH), 1,1-dichloroethane (DCLE) and a mixture of water-acetonitrile was studied (Table 1). The number of molecules in these drops was determined so as for all drops the equimolecular radius[27] is $\approx$ 3.5 nm. The organic molecules were modeled by using the Charmm GENeral Force Field.[49] The dielectric constant and surface tension for the bulk solution were computed and are presented in Table S1 in SI.

In all the systems, all the forces were computed directly without any cut-offs. Equilibrium simulations in NAMD were set by placing the drop in a spherical cavity of radius 20.0 nm by using spherical boundary condition. The cavity was sufficiently large to accommodate the shape fluctuation of the drop. The drop will eventually reach vapor pressure equilibrium. The systems were thermalized with Langevin thermostat with the damping coefficient set to 1/ps. The Rayleigh limit of the drop ($X = 1$ in Eq. 1) was calculated with the surface tension values of the water model used at the simulation temperature.[50] Specifically, for TIP3P at $T = 300$ K the value of surface tension is taken to be 0.0523 N/m and at $T = 350$ K to be 0.0432 N/m.

Ion-ejection simulations from aqueous drops with mixture of ions

Equilibrated drops at $T = 300$ K comprised 6×10^3 H_2O molecules - 10 Na^+ ions - 10 Li^+ (or 10 Cs^+) ions at a temperature 290 K, 300 K, 310 K and 320 K and 330 K were prepared. The ejection of the ions was examined by performing direct MD runs. The software used and details of the MD runs are the same as

3

Table 1: Systems studied, characteristic dimensions and concentrations. n_{H_2O} denotes average number of water molecules and n_I number of ions in the drop during the production runs. R_e [nm] is the equimolecular radius, computed by using density of the TIP3P model at 350 K to be 0.9539 g/cm^3. r_{max} [nm] is the distance from the drop COM to the maximum of the ion concentration profile. λ_{PB} is given in Eq. 2, and the dielectric constant was computed for the solvents used (Table S1). X is the fissility parameter of the simulated drop (Eq. 1). "Range" [nm] denotes the interval defined from the drop COM in which the surface excess charge is located. n_{out} is the number of ions in SECL. Details are presented in the text. C_{SECL} [Molarity] is the ion concentration in the surface excess charge layer.

n_{H_2O}	n_I	R_e	X	r_{max}	λ_{PB}	Range	n_{out}	C_{SECL}(mol/L)
6×10^3	19Na$^+$	3.55	0.85	2.65-2.70	1.41	2.6±0.1-4.4	10.6±0.6	0.062 ±0.004
6×10^3	16His$^+$	3.55	0.62	2.85-2.90	1.68	2.8±0.1-4.6	8.4±0.6	0.044 ±0.002
2×10^4	36Na$^+$	5.31	0.92	4.30-4.35	1.67	4.4±0.1-6.1	13.5±1.0	0.038 ±0.003
2×10^4	36Cs$^+$	5.31	0.92	4.40-4.45	1.67	4.4±0.1-6.1	13.7±1.0	0.038 ±0.003
2×10^4	35Li$^+$	5.31	0.92	4.60-4.65	1.72	4.4±0.1-6.1	15.8±0.8	0.044 ±0.002
2000 ACN	14Na$^+$	3.47	0.66	2.50-2.55	0.323	2.4±0.1-4.6	9.6±0.6	0.045 ±0.003
1500 ACN - 1500 TIP3P	16Na$^+$	3.47	0.86	0.80-0.85	0.512	–	–	–
1300 DCLE	9Na$^+$	3.49	0.40	2.50-2.55	0.192	–	–	–
2600 MeOH	13Na$^+$	3.47	0.72	2.60-2.65	0.466	2.4±0.1-4.6	9.3±0.6	0.044 ±0.003

that described in Sec. "Equilibrium simulations of drops" except that the electrostatic interactions were treated with the multilevel summation method.[51]

Drop disintegration simulations at elevated temperature

Evaporation runs were performed for four systems, for which their initial configurations were comprised (a) $\sim 3 \times 10^4$ H$_2$O, 67 Na$^+$ (or 67 Li$^+$) ions and 23 Cl$^-$ ions (b) $\sim 4 \times 10^3$ H$_2$O - 13 Na$^+$ (or 13 Li$^+$) ions. The initial configurations were equilibrated at 350 K within a spherical cavity of radius 20 nm. The system was re-thermalized at 450 K before the spherical cavity was removed to let the drop evaporate in vacuo. The system temperature was maintained at 450 K for the duration of the production run. The software used and details of the MD runs are the same as that described in Sec. "Equilibrium simulations of drops".

Results and Discussion

Abundance of ions in SECL and ejection mechanism

Figure 1 (a) shows the radial distribution profiles of ions and water molecules in drops comprised 2×10^4 H$_2$O molecules and 36 Na$^+$, 36 Cs$^+$ and 36 Li$^+$ ions. The profiles have been normalized by dividing the raw histogram data with the volume of a spherical shell ($\frac{4}{3}\pi[(r + dr)^3 - r^3]$ where r is the distance from the drop COM). A common feature in all the distributions is that they show a fast exponential decay from their maximum (at r_{max}) followed by a slow decay toward the drop COM. Even though λ_{PB} is an estimate arising from the solution of the non-linear PB equation for a rigid geometry, it predicts well the rapid decay in the systems that we have examined thus far. The maximum of the Li$^+$ distribution is more distant from the drop COM than those of Na$^+$ and Cs$^+$ ions. We attribute this difference to the fact that Li$^+$ tightly bounds its first hydration shell, thus the ion is effectively larger than the Na$^+$ or Cs$^+$
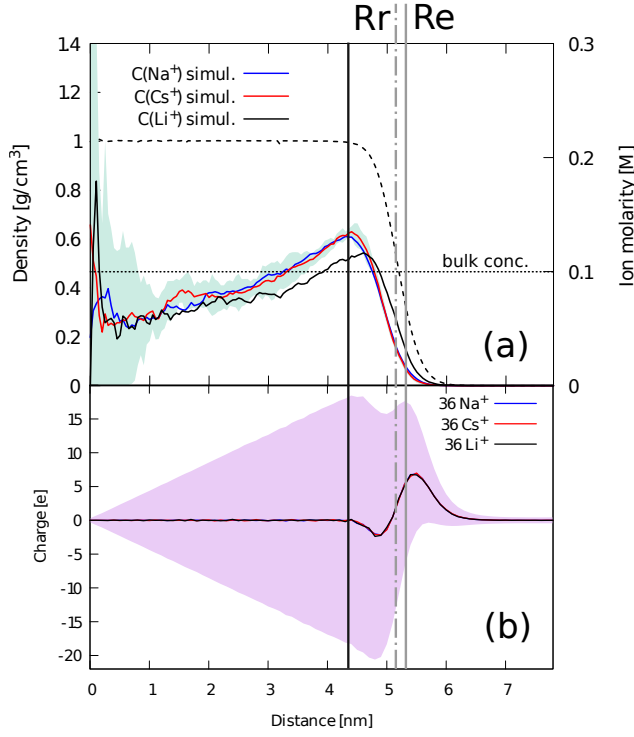
Figure 1: (a) Na^+ (blue), Cs^+ (red), Li^+ (black) radial concentration profiles vs distance from the drop COM for systems comprised 2×10^4 H_2O molecules and 36 ions at $T = 350$ K. The water density is shown by the dashed line and measured in the left axis. The vertical black line marks the distance at which the charge distribution starts to build-up. The horizontal line shows the bulk concentration. (b) Total charge (from the hydrogen, oxygen and ion sites) distribution as a function of distance from the drop COM.

ions.[52–57] The horizontal line (Fig. 1 (a)) marks the bulk concentration, which is simply estimated by the number of ions divided by the volume of the drop (with R_e radius).

Figure 1 (b) shows the radial total charge distribution. The vertical black line marks the distance at which the charge distribution starts to build-up. We find that for Na^+ and Cs^+ ions the 62% of the total number of ions reside in MICR, which is in the interval 3.3 nm-4.7 nm. The excess number of ions relative to the bulk value is 3.5 ions. For Li^+ ions MICR (which is in the interval 4.0 nm-4.9 nm) includes 41%

of the total number of ions. Lithium concentration is lower than that of Na^+ and Cs^+ ions because it has a higher concentration in SECL.

SECL starts approximately at the maximum of the ion distribution for Na^+ and Cs^+ and includes 38% of the ions. For Li^+ ions the maximum of the ion distribution is within the SECL, and it contains 45% of the ions. The combination of data from previous studies[26] and the current study shows that the larger the drop, the smaller the concentration of ions in MICR and SECL when counterions are not present.

Often, the width of the air-water interface is described by the "10-90" thickness rule.[58] For pure water it is approximately 3Å -4Å.[59] In the charged drops the width of this region is ≈ 8 Å and it is determined by shape fluctuations. The width of SECL is broader than the 10-90 interface. Suppression of the shape fluctuations does not affect the decay of the ion distribution. Simulations that we performed in confined liquid with ions in a spherical rigid geometry show similar decay toward the drop interior (Fig. S1 in SI).

The radial ion distribution profile of a drop comprised 6×10^3 H_2O molecules - 16 His^+ ions was also computed (Fig. S2 in SI). We note that long-lived metastable drops with His^+ have less charge than the corresponding sodiated drops, which indicates that His^+ reduces the surface tension of the aqueous drops more than the Na^+ ions. The profile of His^+ shows that the ions are accumulated in MICR. We think that the higher concentration of His^+ in MICR shows the effect of the size of the ions in their location.

The different locations of ions in SECL raises the question of how the equilibrium structure is related to their order of ejection. To examine this question we performed simulations of aqueous drops with mixtures of ions at $T = 300$ K, 310 K, 320 K and 330 K. The simulations consistently showed that solvated Li^+ ions are ejected first. The ejections can takes place as a single solvated Li^+ ion at $T = 300$ K and 310 K. At $T = 320$ K it is possible that two solvated Li^+ ions are released almost simultaneously from diametrically opposed conical protrusions. A typical snapshot of concurrent ejections of two solvated Li^+ ions is shown in Fig. S3 in
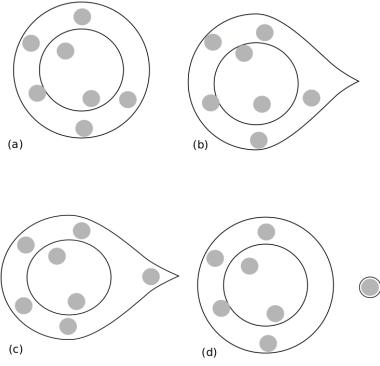
Figure 2: (a)-(d) Schematic sequence of events that lead to the ion release. The region between the internal circle and the outer line delimits the SECL (details in the text).

SI. The formation of the two opposed cones is reminiscent of the jets that have been observed in Rayleigh fission.[60–62] The drops that we study are not large enough to demonstrate the continuous ejection of ions from the cones as it is found in experiments.[60–62] We attribute the formation of two cones to the fact that at the higher temperature, the surface tension of the systems is reduced, which may render the system slightly above the Rayleigh limit. Simulations of drops with mixture of Na^+ and Cs^+ ions show that they are released with the same frequency, which may be a consequence of the identical ion distribution profiles (Fig. 1). The simulations indicate that the ions in abundance within SECL are released first. The most abundant species in SECL is at the same time, the species that are nearer to the drop surface. Contrary to the frequently used non-equilibrium molecular dynamics trajectories in computations related to the analysis of the mass spectrometry signals, the present study demonstrates the significance of the drop equilibrium structure in determining the ion ejection mechanisms. Our finding is consistent with EPM and to our knowledge this is the first direct evidence of the model.

Now, we analyze the ejection mechanism. A charged droplet close to the Rayleigh limit spontaneously develops protuberances similar to the Taylor cones. The solvent shape fluctuations are persistent structures that may or may not contain charged ions. The cones are

in general the locations from where the ions are ejected.

The ejection mechanism follows distinct steps, shown schematically in Fig. 2. The drop undergoes large shape fluctuations that involve the formation of transient cones (Fig. 2 (b)). The cones are the results of global shape fluctuations. The global nature of the shape fluctuation is shown by the fact that if the electrostatic forces are truncated to a distance smaller than the drop radius, the conical shapes do not appear. An ion may diffuse within the cone (Fig. 2 (c)). Once the ion diffuses within the cone it travels toward the tip from where it is released as a small cluster with water (Fig. 2 (d)). In summary, ion ejection takes place when there is a co-operation of events: a cone appears in a location where within its life-time an ion can enter it either by diffusion or by shape fluctuations that engulf the ion in the cone.
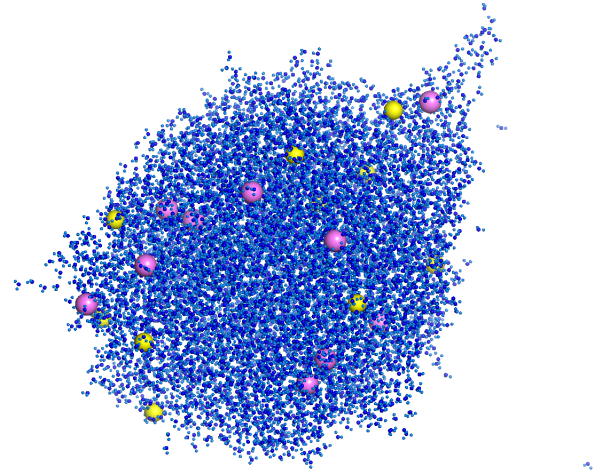

Figure 3: A typical snapshot of a droplet with an emerging conical fluctuation. The drop comprises 5880 TIP3 water molecules, 10 Cs^+ ions (shown in violet) and 10 Na^+ ions (shown in yellow).

We have analysed the dynamics of the protuberances shown in Fig. 3. The drop comprises 5880 TIP3 water molecules, 10 Cs^+ ions (shown in violet) and 10 Na^+ ions (shown in
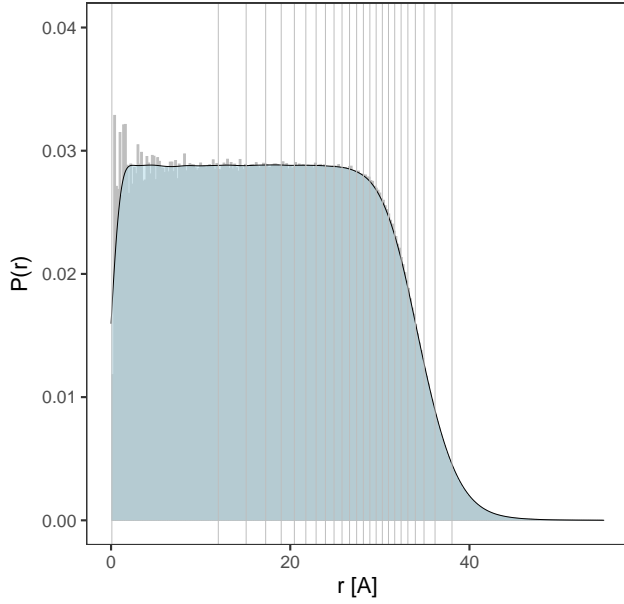
Figure 4: The normalized radial distribution function of the centres of mass of the water molecules corresponding the the system shown in 3.
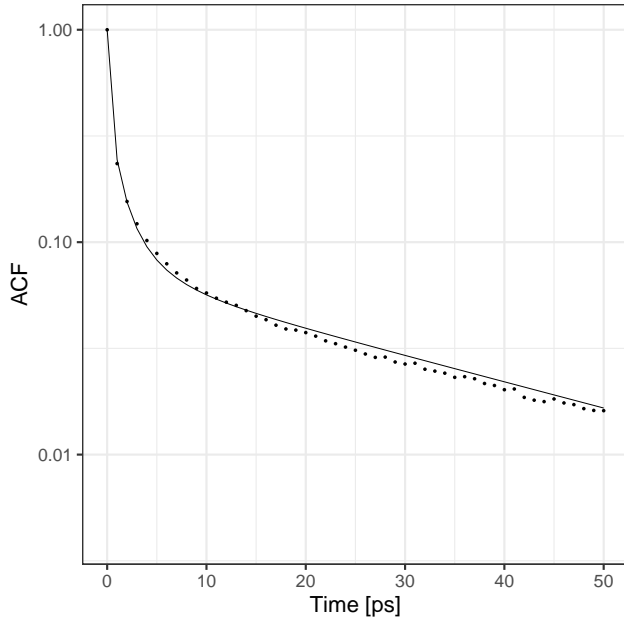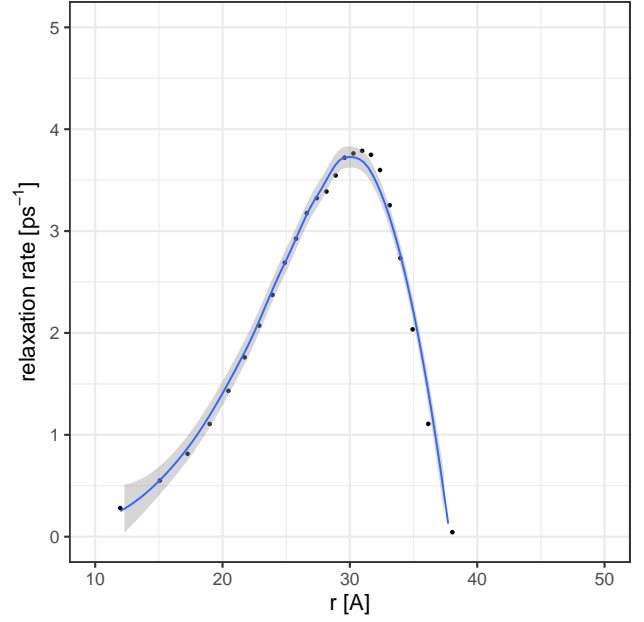

Figure 6: The first relaxation rate of the ACF shown in 5 as a function of shell position (details are presented in the text).

yellow). The system temperature is kept at 330 K. A typical conical formation is clearly seen in the upper right corner of the snapshot. Two ions are present at the foundation of the cone. Monitoring of this cone shows its disappearance within 20 ps without subsequent ion ejection event.

In Fig. 4 we plot the radial distribution function (rdf) of the water molecules' centre of mass obtained during an 1 ns production run. No ion evaporation events were observed during this run. The rdf shows the uniform solvent distribution in the core of the drop and tapered slope at the edge of the drop. The slope is the result of the shape fluctuations of the drop and does not indicate a decrease of the solvent density close to the surface. The vertical lines indicate separation of the drop in equimolar shells at $\{R_1, \ldots, R_n\}$. Every shell $R_k \geqslant \|\mathbf{r}\| \leqslant R_{k+1}$ contains the same number of molecules.

We constructed a state variable for each of the shells

$$
A_k(\mathbf{x}_i(t)) = \begin{cases} 1 & R_k \leqslant \|\mathbf{r}(t)_i\| \leqslant R_{k+1} \\ 0 & \text{otherwise} \end{cases} \quad (3)
$$

where $\mathbf{x}_i$ is the position of the center of mass

Figure 5: Autocorrelation function (ACF) of a shell state variable. The decay is the result of molecule diffusion across the shell boundaries as well as transfer across shells due to some other mechanisms.

of an i-th solvent molecule. We calculated the corresponding auto-correlation functions

$$\text{ACF}_k(\tau) = \langle A_k(\mathbf{x}_i(t+\tau)) A_k(\mathbf{x}_i(t)) \rangle \quad (4)$$

A typical auto-correlation function corresponding the region close the drop surface is plotted in Fig. 5. We numerically fitted the decay function to the following approximation using the R statistical analysis package[63]

$$\text{ACF}_k(\tau) \sim c e^{-\sqrt{r_1\tau}} + (1-c) e^{-r_2\tau} \quad (5)$$

The first term corresponds to a diffusive transfer of molecules across the shell boundaries and the second term corresponds to a regular Markov process. The fit captures the general shape of the ACF decay indicating that the above two mechanisms account for the solvent transfer between the shells.

In Fig. 6 we plot the first relaxation rate r_1 as a function of the shell position. In the plot, we observe that for the region, where the conical shape fluctuations are observed, the first relaxation rate has small values. This may account for a long life of the emerging protuberances.

The finding of the cones is consistent with our previous research where we approached the problem of the ion release from drops using a different methodology.[24] In that study, we computed the free energy of detachment of a solvated ion from a parent drop along a collective reaction coordinate, which takes into account the position of all the solvent molecules and ions. We found that an ion may be ejected from a conical formation that corresponds to the barrier top of the free energy profile along this reaction coordinate.[24,64]

Generally, from the simulation studies we cannot infer whether the release of ions from small nanodrops follows the ion evaporation mechanism[28–30] (IEM) or Rayleigh fission. It has been found in experiments that Rayleigh fission of aqueous microdrops releases 20%-40% of charge.[65] In a drop of up to a few thousands of water molecule, this percentage corresponds to only a few ions. The scaling of the data implies that the observation of the single-ion ejection from a minute nanodrop does not warrant an IEM mechanism. Our view is different from that that has been presented in the literature.[66] We elaborate more on this point in the next section. We have also observed in simulations (see Table 1 and Ref.[26]) and we justify it in the Appendix that the smaller a drop the smaller the X value in which it settles in a quasi-equilibrium state. The fact that a drop of a few thousand of water molecules ejects ions much before the Rayleigh limit, is consistent with the Rayleigh fluctuations (see Appendix), therefore, the ejection of ions cannot be differentiated from a Rayleigh mechanism.
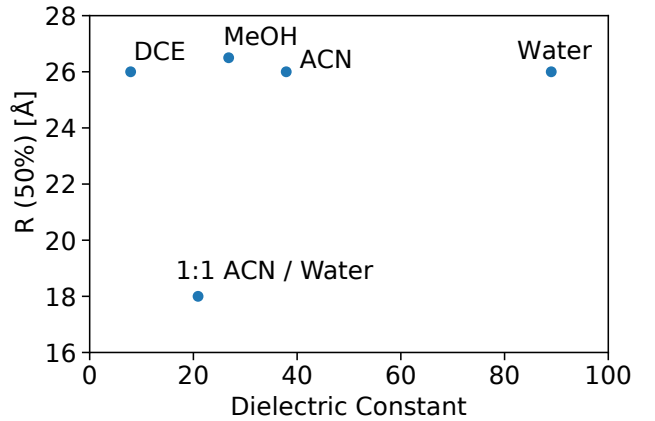
Solvents with $\varepsilon < \varepsilon_{H_2O}$

Figure 7: Drop radius that divides in half the number of ions as a function of the solvent's dielectric constant. The systems are presented in Table 1.

The Na$^+$ radial ion distribution in drop with lower dielectric constant than water were computed. All the systems have approximately the same R_e (Table 1). It is found that regardless of the dielectric constant the distance that divides the 50% of the ions is the same. Among all single-solvent drops we have tested, the solvent density dies off to 5×10^{-4} g/cm^3 at approximately 1.9 nm from the Na$^+$ concentration maximum.

The charge distribution profile in these drops was examined (Fig. S4, S5, S6 in SI). An undulated function appear when the solvent density sharply declines in acetonitrile drop and methanol drop. In both drops, the charge
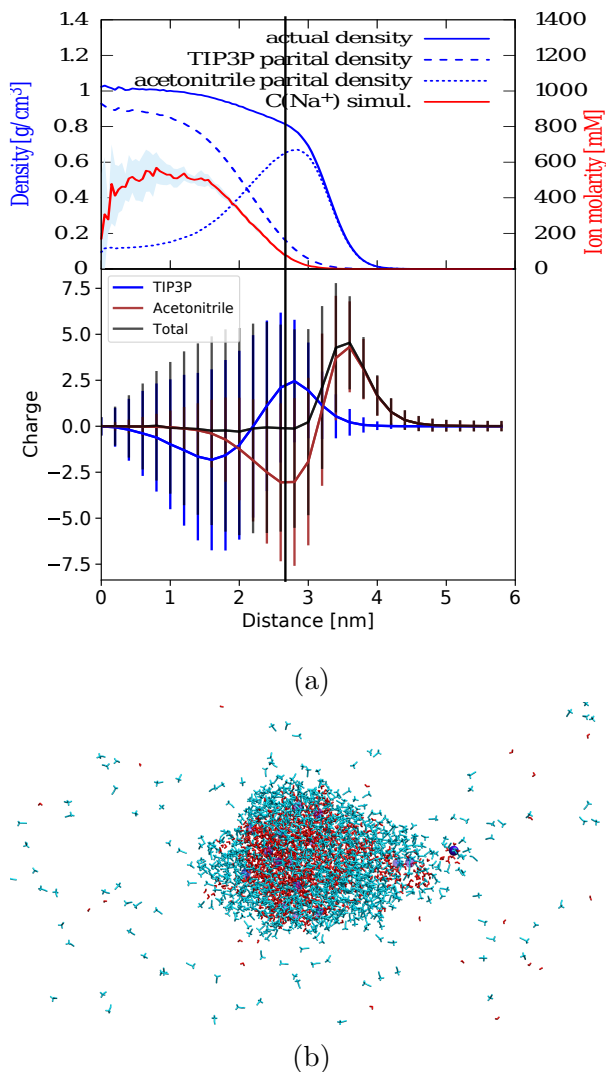
(a)

(b)

Figure 8: (a) Same as Fig. 1 but for a drop ($R_e \approx 3.5$ nm) comprising acetonitrile, water molecules and sodium ions at 300 K. (b) Typical snapshot of Na$^+$ (blue sphere) ejection from a H$_2$O (red colored core)-ACN (light blue colored outer layer) drop.

minimum and maximum appears at 2.8 nm and 3.6 nm, respectively. Compared with the aqueous drop with similar volume (comprised ≈ 6000 H$_2$O molecules), the charge minimum in acetonitrile drop is closer to COM and the maximum is located at almost the same place.[25] However, a undulated function is not found in the total charge profile of the 1,1-dichloroethane drop, and therefore, only a maximum is observed at 3.2 nm.

Figure 8 (a) shows the radial ion distribution,

the acetonitrile partial density profile, the water partial density profile and the Na$^+$ charge profile for a drop of 1500 CH$_3$CN molecules, 1500 H$_2$O molecules and 16 Na$^+$ ions. The partial density of water is calculated by considering only water molecules and excluding the acetonitrile molecules in the computation of density, and vice versa. Therefore the actual density is the sum of the partial densities of TIP3P and acetonitrile. The partial density of H$_2$O in the interior part of the drop is higher than in the outer part, while the density of CH$_3$CN follows the opposite trend. Contrary to the acetonitrile drops, the Na$^+$ ions tends to be located in the interior part of the drop and its concentration reaches its maximum at about 0.8 nm from the COM, where the partial density of water is higher than the partial density of acetonitrile. The density in this drop dies off to 5×10^{-4} g/cm^3 at approximately 3.7 nm from the Na$^+$ concentration maximum.

Figure 8 (b) shows the charge distribution profile in the drop. The total profile is dominated by a positive peak. An incipient negative trough appears at ≈ 2.8 nm.

The ejection of ions is shown in Fig. 8 (b). The water molecules make a path within the ACN for the ion to be released.

Limitations of atomistic simulations in detecting IEM

Simulations were performed at elevated temperature in order to examine the relation between the ion ejection mechanism and the structure of the drop outer layer when solvent evaporation rate is higher than the ion diffusion rate. Accumulation of analytes on the drop surface because of rapid solvent evaporation has often been speculated to explain the mechanisms by which the species detected in mass spectrometry are formed. Higashi et al. have performed atomistic simulations at $T = 460$ K of charged nanodrops comprised 2500 and 1000 H$_2$O molecules, Na$^+$ ions and Cl$^-$ ions in order to provide direct evidence of the IEM.[66] Temperature determines to a great extent the events

in a drop's lifetime. Even though temperature of $T = 460$ K in simulations appears to be high it is still not clear whether it is unrealistic because of conflicting experimental data on drop temperature.[67,68]

In general, drop temperature will depend on the details of the instrument and the specific experiment. A drop within a background gas and a partial pressure less than the equilibrium vapour pressure, will cool down due to evaporation. Antoine et al. have found by using laser-induced fluorescence and Mie scattering measurements that the temperature of electrosprayed microdrops increases to 307 K.[67] The increase is attributed to the conductive thermal transfer with the sheath gas. Cook et al. use a different experimental set-up and they find that microdrops cool initially by 30 K.[68] Beauchamp et al. have noted that time required for the velocity redistribution between the drop outer layers and deep interior may lead to a colder surface.[65,69] In the small nano-drops, the velocity redistribution will be rapid, thus a uniform temperature can be established.

In our simulations we choose as an initial condition a configuration taken from the equilibrium ensemble. The simulations have been performed by placing the drop in vacuo and thermalizing it at $T = 450$ K. In order to analyze the location of ions in a rapidly evaporating drop the trajectory of the simulation was separated into blocks between ion evaporation events. In the blocks the number of H_2O molecules and ions in the drop does not change considerably. The radial ion distributions and the water denisty in representative blocks are shown in Fig. 9.

At $T = 450$ K, the average water density in the interior of the water is 0.89 g/mL, which is significantly lower than the water density at room temperature. The water-air interface is significantly wider ≈ 3.0 nm at 450 K compared to 1.5 nm-1.7 nm at $T = 350$ K. The distance between the water density and the ion concentration profile in the 10-90 interface gradually decreases as the drop shrinks. This increase indicates that the rate of solvent evaporation is higher than the rate of ion diffusion.

Figure 10 (a) shows the evolution of drop size

and charge as a function of time and Fig. 10 (b) the time evolution of the fissility parameter. The trend is the same in drops comprised 3×10^4 and 4×10^3 H_2O that we investigated (Fig. S7, S8 in SI). However, the smaller drop may reach states with $X = 1.2$ relative to the larger drop that reaches states with $X = 1.6$. Interestingly, the drops with Na^+ and Li^+ ions show the same fragmentation pattern. This is in agreement with the Rayleigh continuum model that does not differentiate the nature of the ions. These findings show that the drops can be found transiently above the Rayleigh limit before they fragment. We note that IEM should occur before the Rayleigh limit, therefore, IEM cannot be the mechanism that is followed when drops are found above the Rayleigh limit.

Transient drop states above the Rayleigh limit have been detected in experiments. Beauchamp et al.[69] have reported that methanol microdrops with a small percentage of certain additive may fragment in a range of 112%-135% above the Rayleigh limit. This range corresponds to fissility parameter 1.25-1.825. Beauchamp et al.[65,69] consider the temperature of the drop to be that of the background gas, which is reported to be as high as 328 K. It is not clear whether at 328 K temperature may not lead to faster solvent evaporation than ion diffusion. We propose that in addition to the temperature of the background gas friction is another factor that may lead to the increase in the drop temperature.

Now, we examine the reason that drops can transiently reach states above the Rayleigh limit.

At the elevated temperature the Rayleigh limit may not hold because there is no surface tension since the drops are found at a temperature above the solvent's boiling temperature. The H_2O molecules are highly polarized in a thick outer drop layer. This layer creates a cage for the ions that delays their release. In this study, we examined how ions are emitted from the conical protrusions that appear in the drop surface in $T = 300$ K-330 K. This observation is also supported by other works that they have found experimentally and computationally that conical drop deformations of a neutral drop

in an external electric field[70] or via Rayleigh mechanism[60,62] play a key role in the release of ions. In the high temperature, incipient cones rapidly undergo a death and birth process in different locations on the drop surface. The ions do not diffuse fast enough to enter the cones. Therefore, one of the release mechanisms for ions is less likely to be followed.

Higashi et al. have found excellent agreement of MD simulations evaporation simulations at $T = 460$ K with the Labowsky et al. model[30] of IEM.[66] The simulated drops comprise 2500 and 1000 water molecules with Na^+ and Cl^- ions at a concentration that the solution is supersaturated. In light of our findings, the agreement between simulations and the Labowsky et al. model gives rise to a striking paradox. The main assumptions of the Labowsky et al. model are that (a) the free energy of activation arises from the Born ion solvation model and surface energy, which are equilibrium quantities, (b) all the ions are on the surface and (c) the charge of the ions is screened by the solvent, thus every solvated ion is not affected by the charge of the other ions. Under the conditions of the simulations the assumptions of the Labowsky et al. model may not hold because (a) as we showed at 450 K the ion distributions do not relax to equilibrium when solvent evaporation is faster than the diffusion of ions toward the drop interior. (b) in solution of high ion concentration as that of the simulations, ions share their solvation shell, thus, these solutions are characterized by low dielecric constant and the charge of the ions may not be screened by water in the smallest drops of 1000 H_2O molecules.[27,71–77] (c) Here we showed that small drops at elevated temperature can be found above the Rayleigh limit, which contradicts the fact that IEM takes place below the Rayleigh limit.

In summary we demonstrate that simulations under conditions where the solvent evaporation is faster than the ion diffusion can lead to transient above the Rayleigh limit drop states. This finding may provide insight to experimental observations that find drop states above the Rayleigh limit before fragmentation. Simulations of release of ions from small nanodrops at elevated temperature cannot provide evidence that an ion-evaporation mechanism and its continuum modeling hold.

Conclusion

The relation between the ion composition of the electric double layer in drops and the ion-ejection mechanisms was examined. A distinct example is the order of ejection of of Li^+, Na^+ and Cs^+ ions in drops with mixture of ions. The SECL is enriched in Li^+ ions relative to Na^+ at the same concentration. In evaporation runs, Li^+ ions are ejected earlier. This is the first direct evidence to support the equilibrium partition model of Enke. The lower the dielecric constant of a solvent, the width of the SECL increases. In mixture of solvents, CH_3CN-H_2O with Na^+ ions, the water is found in the drop center and contains the ions. The ions are released by the penetration of a water string within the CH_3CN outer layer, that provides the path for their release.

Rapid evaporation of charged drops consistently show that the systems can be found above the Rayleigh limit before they fragment. We attribute the delay in the ion release to two factors (a) the Rayleigh theory may not hold under the elevated temperature because the surface tension is not defined under these conditions (b) the short life-time of the conical deformations on the drop surface relative to the diffusion time of the ions to the conical tips prevents the ions to follow one of their ejection paths that is followed at lower temperature. The finding may provide insight to experiments that have detected drops above the Rayleigh limit before fission.

The small drop size or enrichment of the outer solvent layers in ions under rapid evaporation signals caution when simulations of minute nanodrops at elevated temperature are used to validate models of the ion evaporation mechanism.[66] When evaporation is fast ions reside in non-equilibrium positions in the drop periphery. Thus, their solvation does not obey the Born solvation model that underlies the ion evaporation models. In nano-drops, there is a distinct MICR and a SECL which overlap. SECL is the
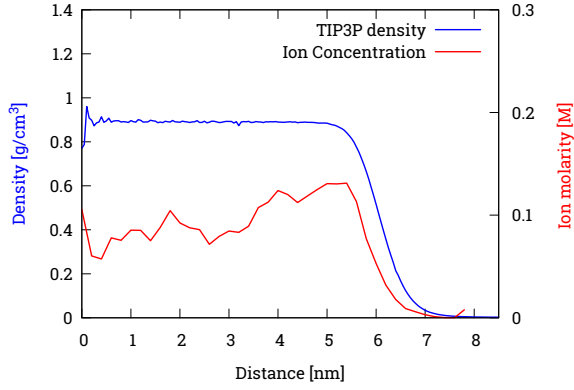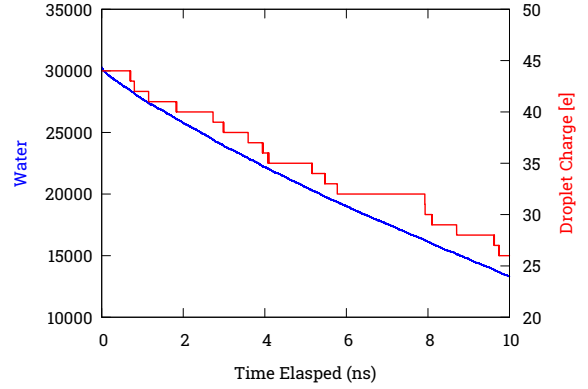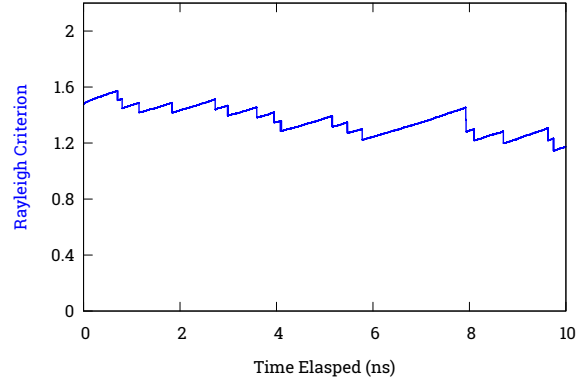
(a)
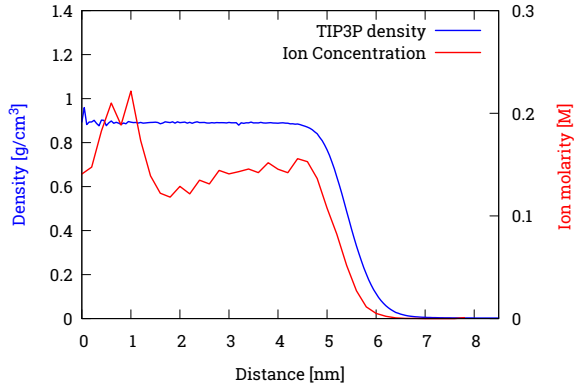
(b)
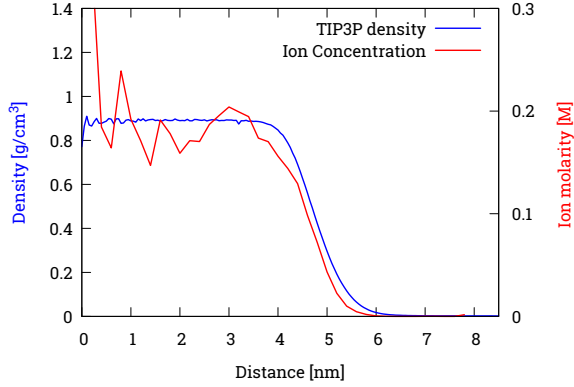
(c)

Figure 9: Water density and ion concentration profile of the drop comprised (a) 67 Na^+-23 Cl^- ions and $2.84 \times 10^4 - 3.03 \times 10^4$ H_2O molecules averaged over a time period of 1.409 ns, (b) 58 Na^+ - 23 Cl^- ions and $2.03 \times 10^4 - 2.2 \times 10^4$ H_2O molecules averaged over a time period of 2.11 ns and (c) 51 Na^+ 23 Cl^- ions and $1.38 \times 10^4 - 1.51 \times 10^4$ H_2O molecules averaged over a time period 1.851 ns.

(a)

(b)

Figure 10: Evolution of an evaporating drop composed of 3×10^4 H_2O molecules - 44 Na^+ ions - NaCl pairs at $T = 450$ K. (a) evolution of number of H_2O molecules and drop charge (b) Fissility parameter (X) as a function of time.

layer where chemical reactions that occur in the interface with vapor may couple to the drop shape fluctuations. This coupling may play a more significant role in mesoscopic drops. The composition of SECL also determines the type of ions that are ejected. Thus, SECL composition should be taken into account when examining release of small ionic species that are detected by mass spectrometry. The concentration of ions in MICR and SECL is higher in nano-drops than in micro-drops. The presence of counterions will increase the excess ion concentration in MICR.

Although in principle atomistic simulations appear to be the method that allows for the direct capture of the fission events, the simulations may be misleading because the final residue of non-equilibrium molecular dynamics trajectories depend on the history of the drop. We have argued in previous articles that drops of diameter of at least 20 nm should be simulated in order to determine the states of macromolecules.[25]

In order to study the reactivity in electrosprayed drops, it will be insightful to perform experiments in mixture of solvents that can create a bilayer system, such as H_2O and CH_3CN in the presence of ions. This system may reveal the role of interfaces in altering reactivity.

The next question to address is how the presence of macromolecules may affect the preferential release of ions. Synergy of experiments and computations in exploring the effect of the mixture of ions in the charging of macromolecules and their ejection may provide insight into the charging mechanisms of macromolecules. We suggest Li^+ to be one of the candidate ions to use in experiments because its spatial distribution is clearly different from that of the other alkali metals and it also shares commonalities with the hydronium ions.

The use of supervised and unsupervised machine learning has opened up new possibilities and interpretations in mass spectrometry imagining where a plethora of data are available.[78–83] Similarly, we envision that a database of experimental and computational ion distributions and macroions in SECL may relate its composition to the mass spectrum.

Appendix

In all the simulations present and in previous research, we have found that the larger a drop the closer to $X = 1$ can exist for a longer period of time. The explanation of this behavior is as follows: The surface can be expressed as:

$$\rho(\omega) = R + \sum_{l>0,m_l} a_{l,m_l} Y_{l,m_l}(\omega) \qquad (6)$$

where $\omega = (\theta, \phi)$ is the spherical angle, $\rho(\omega)$ is the distance from the centre, and $Y_{lm_l}(\omega)$ denote the spherical harmonics functions of rank m and order l. R is the $l = 0$ term in the expansion of $\rho(\omega)$ and a_{lm_l} are the amplitudes in the expansion of the surface fluctuations in terms of spherical harmonics. For certain shapes of drops, such as bottle-necked shapes or "eight"-like shapes we should choose the center of the shape carefully, so as we do not have for a single (θ, ϕ) more than one values of ρ. Equation 6 can also be written as

$$\rho(\omega) = R \left[1 + \sum_{l>0,m_l} \frac{a_{l,m_l}}{R} Y_{l,m_l}(\omega) \right] \qquad (7)$$

If we assume the same mechanism that leads to drop break-up for the smaller and larger drops, then a_{l,m_l} is proportional to R. We make the above statement for the unstable modes, $l = 2$ or in general for the modes that are important for drop fragmentation. Maybe this assumption is not true for all the modes.

In a macroscopic description, the change in free energy of a drop due to a perturbation from the spherical shape (but with fixed volume), can be expressed to lowest order as[36,38]

$$\delta E = (2\pi R_0^2 \gamma) \qquad (8)$$

$$\sum_{l>0 \wedge |m| \leq l} (l-1) \left[(l+2) - \frac{Q^2}{(4\pi)^2 \varepsilon_0 R_0^3 \gamma} \right] |a_{lm_l}|^2 \qquad (9)$$

where Q, R_0, and γ denote the total charge of the drop, the unperturbed drop radius, and the surface tension, respectively, and ε_0 is the permittivity of vacuum.

Equation 8 can also be written as

$$\delta E = (2\pi R_0^2 \gamma) \sum_{l>0 \wedge |m_l| \leq l} (l-1)\left[(l+2) - 4X\right]|a_{lm}|^2 \tag{10}$$

$$= (2\pi R_0^2 \gamma) \sum_{l>0 \wedge |m_l| \leq l} \eta_{lm_l}|a_{lm_l}|^2 \tag{11}$$

where X is the fissility parameter and $\eta_{lm_l} = (l-1)[(l+2)-4X]$.

The charged drops are metastable states even if they are much below the Rayleigh limit. We compare two drops with radii R' and R''. The rate constant is given by

$$k(R) \sim \exp(-E^*/k_B T) \tag{12}$$

We take the rate of fragmentation to be the same in drops of different size, thus,

$$k(R') \sim k(R'') \Rightarrow \eta_{lm}(R')|a'_{lm}|^2 \sim \eta_{lm}(R'')|a''_{lm}|^2 \tag{13}$$

If the same mechanism of break-up holds, i.e. the same fluctuations appear in the barrier top, then, $a_{l,m_l}/R$ is a constant. Then, Eq. 13 for $l = 2$ becomes

$$\eta_{lm}(R')R'^2 \sim \eta_{lm}(R'')R''^2 \Rightarrow \frac{1-X'}{1-X''} \sim \left(\frac{R''}{R'}\right)^2 \tag{14}$$

Therefore, the smaller the drop the smaller the X for fragmentation.

Conflict of interest The authors declare no conflict of interest.

References

(1) Shi, Z.; Tan, Y.; Tang, H.; Sun, J.; Yang, Y.; Peng, L.; Guo, X. Aerosol effect on the land-ocean contrast in thunderstorm electrification and lightning frequency. *Atmos. Res.* **2015**, *164*, 131–141.

(2) Yudistira, H. T.; Nguyen, V. D.; Dutta, P.; Byun, D. Flight behavior of charged droplets in electrohydrodynamic inkjet printing. *Appl. Phys. Lett.* **2010**, *96*, 023503.

(3) Bain, R. M.; Pulliam, C. J.; Cooks, R. G. Accelerated Hantzsch electrospray synthesis with temporal control of reaction intermediates. *Chem. Sci.* **2015**, *6*, 397–401.

(4) Ingram, A. J.; Boeser, C. L.; Zare, R. N. Going beyond electrospray: mass spectrometric studies of chemical reactions in and on liquids. *Chem. Sci.* **2016**, *7*, 39–55.

(5) Malik, S. A.; Ng, W. H.; Bowen, J.; Tang, J.; Gomez, A.; Kenyon, A. J.; Day, R. M. Electrospray synthesis and properties of hierarchically structured PLGA TIPS microspheres for use as controlled release technologies. *J. Colloid Interface Sci.* **2016**, *467*, 220–229.

(6) Chen, X.; Cooks, R. G. Accelerated reactions in field desorption mass spectrometry. *J. Mass Spectrom.* **2018**, *53*, 942–946.

(7) Schrader, R. L.; Fedick, P. W.; Mehari, T. F.; Cooks, R. G. Accelerated Chemical Synthesis: Three Ways of

Performing the Katritzky Transamination Reaction. *J. Chem. Educ.* **2019**,

(8) Lee, J. K.; Banerjee, S.; Nam, H. G.; Zare, R. N. Acceleration of reaction in charged microdroplets. *Q. Rev. Biophys.* **2015**, *48*, 437–444.

(9) Sahraeian, T.; Kulyk, D. S.; Badu-Tawiah, A. K. Droplet Imbibition Enables Non-Equilibrium Interfacial Reactions in Charged Microdroplets. *Langmuir* **2019**,

(10) Kulyk, D. S.; Miller, C. F.; Badu-Tawiah, A. K. Reactive charged droplets for reduction of matrix effects in electrospray ionization mass spectrometry. *Analytical chemistry* **2015**, *87*, 10988–10994.

(11) Rovelli, G.; Jacobs, M. I.; Willis, M. D.; Rapf, R. J.; Prophet, A. M.; Wilson, K. R. A critical analysis of electrospray techniques for the determination of accelerated rates and mechanisms of chemical reactions in droplets. *Chem. Sci.* **2020**, *11*, 13026–13043.

(12) Loo, R. R. O.; Lakshmanan, R.; Loo, J. A. What protein charging (and supercharging) reveal about the mechanism of electrospray ionization. *Journal of the American Society for Mass Spectrometry* **2014**, *25*, 1675–1693.

(13) Mehmood, S.; Allison, T. M.; Robinson, C. V. Mass spectrometry of protein complexes: From origins to applications. *Annu. Rev. Phys. Chem.* **2015**, *66*, 453–474.

(14) Hirabayashi, A.; Sakairi, M.; Koizumi, H. Sonic spray ionization method for atmospheric pressure ionization mass spectrometry. *Anal. Chem.* **1994**, *66*, 4557–4559.

(15) Blakley, C.; Vestal, M. Thermospray interface for liquid chromatography/mass spectrometry. *Anal. Chem.* **1983**, *55*, 750–754.

(16) Monge, M. E.; Harris, G. A.; Dwivedi, P.; Fernandez, F. M. Mass spectrometry: recent advances in direct open air surface sampling/ionization. *Chem. Rev.* **2013**, *113*, 2269–2308.

(17) Teunissen, S. F.; Eberlin, M. N. Transferring Ions from Solution to the Gas Phase: The Two Basic Principles. *J. Am. Soc. Mass Spectrom.* **2017**, *28*, 2255–2261.

(18) Sakairi, M.; Kambara, H. Atmospheric pressure spray ionization for liquid chromatography/mass spectrometry. *Anal. Chem.* **1989**, *61*, 1159–1164.

(19) Bruins, A. P.; Covey, T. R.; Henion, J. D. Ion spray interface for combined liquid chromatography/atmospheric pressure ionization mass spectrometry. *Anal. Chem.* **1987**, *59*, 2642–2646.

(20) Kambara, H. Sample introduction system for atmospheric pressure ionization mass spectrometry of nonvolatile compounds. *Anal. Chem.* **1982**, *54*, 143–146.

(21) de la Mora, J. F. Electrospray ionization of large multiply charged species proceeds via Dole's charged residue mechanism. *Anal. Chim. Acta* **2000**, *406*, 93–104.

(22) Wilm, M. Principles of electrospray ionization. *Mol. Cell. Proteomics* **2011**, *10*, M111–009407.

(23) Kebarle, P.; Verkerk, U. H. Electrospray: from ions in solution to ions in the gas phase, what we know now. *Mass Spectrom. Rev.* **2009**, *28*, 898–917.

(24) Consta, S.; Mainer, K. R.; Novak, W. Fragmentation mechanisms of aqueous clusters charged with ions. *J. Chem. Phys.* **2003**, *119*, 10125–10132.

(25) Kwan, V.; Malevanets, A.; Consta, S. Where do the ions reside in a highly charged droplet? *J. Phys. Chem. A* **2019**, *123*, 9298–9310, PMID: 31589448.

(26) Kwan, V.; Consta, S. Bridging electrostatic properties between nanoscopic and microscopic highly charged droplets. *Chem. Phys. Lett.* **2020**, *746*, 137238.

(27) Kwan, V.; Consta, S. Molecular Characterization of the Surface Excess Charge Layer in Droplets. *J. Am. Soc. Mass Spectrom.* **2021**, *32*, 33–45.

(28) Iribarne, J. V.; Thomson, B. A. On the evaporation of small ions from charged droplets. *J. Chem. Phys.* **1976**, *64*, 2287–2294.

(29) Thomson, B.; Iribarne, J. Field induced ion evaporation from liquid surfaces at atmospheric pressure. *J. Chem. Phys.* **1979**, *71*, 4451–4463.

(30) Labowsky, M.; Fenn, J.; de la Mora, J. F. A continuum model for ion evaporation from a drop: effect of curvature and charge on ion solvation energy. *Anal. Chim.* **2000**, *406*, 105–118.

(31) Enke, C. G. A predictive model for matrix and analyte effects in electrospray ionization of singly-charged ionic analytes. *Analytical Chemistry* **1997**, *69*, 4885–4893.

(32) Constantopoulos, T. L.; Jackson, G. S.; Enke, C. G. Challenges in achieving a fundamental model for ESI. *Analytica Chimica Acta* **2000**, *406*, 37–52.

(33) Malevanets, A.; Consta, S. Variation of droplet acidity during evaporation. *J. Chem. Phys.* **2013**, *138*, 184312.

(34) Chamberlayne, C. F.; Zare, R. N. Simple model for the electric field and spatial distribution of ions in a microdroplet. *J. Chem. Phys.* **2020**, *152*, 184702.

(35) Rayleigh, L. XX. On the equilibrium of liquid conducting masses charged with electricity. *Philos. Mag.* **1882**, *14*, 184–186.

(36) Hendricks, C.; Schneider, J. Stability of a conducting droplet under the influence of surface tension and electrostatic forces. *Am. J. Phys* **1963**, *31*, 450–453.

(37) Peters, J. Rayleigh's electrified water drops. *Eur. J. Phys.* **1980**, *1*, 143.

(38) Consta, S.; Malevanets, A. Disintegration mechanisms of charged nanodroplets: novel systems for applying methods of activated processes. *Mol. Simul.* **2015**, *41*, 73–85.

(39) Oh, M. I.; Malevanets, A.; Paliy, M.; Frenkel, D.; Consta, S. When droplets become stars: charged dielectric droplets beyond the Rayleigh limit. *Soft Matter* **2017**, *13*, 8781–8795.

(40) Labowsky, M. Discrete charge distributions in dielectric droplets. *J. Colloid Interface Sci.* **1998**, *206*, 19–28.

(41) Phillips, J. C.; Braun, R.; Wang, W.; Gumbart, J.; Tajkhorshid, E.; Villa, E.; Chipot, C.; Skeel, R. D.; Kalé, L.; Schulten, K. Scalable molecular dynamics with NAMD. *J. Comput. Chem.* **2005**, *26*, 1781–1802.

(42) Humphrey, W.; Dalke, A.; Schulten, K. VMD: Visual Molecular Dynamics. *J. Mol. Graphics* **1996**, *14*, 33–38.

(43) Jorgensen, W. L.; Jenson, C. Temperature dependence of TIP3P, SPC, and TIP4P water from NPT Monte Carlo simulations: Seeking temperatures of maximum density. *J. Comput. Chem.* **1998**, *19*, 1179–1186.

(44) Abascal, J. L. F.; Vega, C. A general purpose model for the condensed phases of water: TIP4P/2005. *J. Chem. Phys.* **2005**, *123*, 234505.

(45) Noskov, S. Y.; Roux, B. Control of Ion Selectivity in LeuT: Two Na+ Binding Sites with Two Different Mechanisms. *J. Mol. Biol.* **2008**, *377*, 804 – 818.

(46) Beglov, D.; Roux, B. Finite representation of an infinite bulk system: Solvent boundary potential for computer simulations. *J. Chem. Phys.* **1994**, *100*, 9050–9063.

(47) Chandrasekhar, J.; Spellmeyer, D. C.; Jorgensen, W. L. Energy component analysis for dilute aqueous solutions of lithium(1+), sodium(1+), fluoride(1-), and chloride(1-) ions. *J. Am. Chem. Soc.* **1984**, *106*, 903–910.

(48) McDonald, N. A.; Duffy, E. M.; Jorgensen, W. L. Monte Carlo investigations of selective anion complexation by a bis(phenylurea) p-tert-butylcalix[4]arene. *J. Am. Chem. Soc.* **1998**, *120*, 5104–5111.

(49) Vanommeslaeghe, K.; Hatcher, E.; Acharya, C.; Kundu, S.; Zhong, S.; Shim, J.; Darian, E.; Guvench, O.; Lopes, P.; Vorobyov, I. et al. CHARMM general force field: A force field for drug-like molecules compatible with the CHARMM all-atom additive biological force fields. *J. Comp. Chem.* **2010**, *31*, 671–690.

(50) Vega, C.; de Miguel, E. Surface tension of the most popular models of water by using the test-area simulation method. *J. Chem. Phys.* **2007**, *126*, 154707.

(51) Hardy, D. J.; Wu, Z.; Phillips, J. C.; Stone, J. E.; Skeel, R. D.; Schulten, K. Multilevel summation method for electrostatic force evaluation. *J. Chem. Theory Comput.* **2015**, *11*, 766–779.

(52) Lyubartsev, A.; Laasonen, K.; Laaksonen, A. d. Hydration of Li+ ion. An ab initio molecular dynamics simulation. *J. Chem. Phys.* **2001**, *114*, 3120–3126.

(53) Pye, C. C.; Rudolph, W.; Poirier, R. A. An ab initio investigation of lithium ion hydration. *J. Phys. Chem.* **1996**, *100*, 601–605.

(54) Rudolph, W.; Brooker, M. H.; Pye, C. C. Hydration of lithium ion in aqueous solutions. *J. Phys. Chem.* **1995**, *99*, 3793–3797.

(55) Loeffler, H. H.; Rode, B. M. The hydration structure of the lithium ion. *J. Chem. Phys.* **2002**, *117*, 110–117.

(56) Newsome, J.; Neilson, G.; Enderby, J. Lithium ions in aqueous solution. *J. Phys. C* **1980**, *13*, L923.

(57) Matsuda, Y.; Fukushima, T.; Hashimoto, H.; Arakawa, R. Solvation of lithium ions in mixed organic electrolyte solutions by electrospray ionization mass spectroscopy. *J. Electrochem. Soc.* **2002**, *149*, A1045.

(58) Lekner, J.; Henderson, J. Theoretical determination of the thickness of a liquid-vapour interface. *Physica A: Statistical Mechanics and its Applications* **1978**, *94*, 545–558.

(59) Zakharov, V. V.; Brodskaya, E. N.; Laaksonen, A. Surface tension of water droplets: A molecular dynamics study of model and size dependencies. *J. Chem. Phys.* **1997**, *107*, 10675–10683.

(60) Gomez, A.; Tang, K. Charge and fission of droplets in electrostatic sprays. *Phys. Fluids* **1994**, *6*, 404–414.

(61) Duft, D.; Lebius, H.; Huber, B. A.; Guet, C.; Leisner, T. Shape Oscillations and Stability of Charged Microdroplets. *Phys. Rev. Lett.* **2002**, *89*, 084503.

(62) Duft, D.; Achtzehn, T.; Muller, R.; Huber, B. A.; Leisner, T. Coulomb fission: Rayleigh jets from levitated microdroplets. *Nature* **2003**, *421*, 128–128.

(63) R Core Team, R: A Language and Environment for Statistical Computing. R Foundation for Statistical Computing: Vienna, Austria, 2017.

(64) Consta, S. Fragmentation reactions of charged aqueous clusters. *J. Mol. Struct. THEOCHEM* **2002**, *591*, 131–140.

(65) Smith, J. N.; Flagan, R. C.; Beauchamp, J. Droplet evaporation and discharge dynamics in electrospray ionization. *J. Phys. Chem. A* **2002**, *106*, 9957–9967.

(66) Higashi, H.; Tokumi, T.; Hogan, C. J.; Suda, H.; Seto, T.; Otani, Y. Simultaneous ion and neutral evaporation in aqueous nanodrops: experiment, theory, and molecular dynamics simulations. *Phys. Chem. Chem. Phys.* **2015**, *17*, 15746–15755.

(67) Soleilhac, A.; Dagany, X.; Dugourd, P.; Girod, M.; Antoine, R. Correlating droplet size with temperature changes in electrospray source by optical methods. *Anal. Chem.* **2015**, *87*, 8210–8217.

(68) Gibson, S. C.; Feigerle, C. S.; Cook, K. D. Fluorometric measurement and modeling of droplet temperature changes in an electrospray plume. *Anal. Chem.* **2013**, *86*, 464–472.

(69) Grimm, R. L.; Beauchamp, J. Evaporation and discharge dynamics of highly charged multicomponent droplets generated by electrospray ionization. *J. Phys. Chem. A* **2009**, *114*, 1411–1419.

(70) Luedtke, W. D.; Landman, U.; Chiu, Y.-H.; Levandier, D. J.; Dressler, R. A.; Sok, S.; Gordon, M. S. Nanojets, Electrospray, and Ion Field Evaporation: Molecular Dynamics Simulations and Laboratory Experiments. *J. Phys. Chem. A* **2008**, *112*, 9628–9649.

(71) Gavish, N.; Promislow, K. Dependence of the dielectric constant of electrolyte solutions on ionic concentration: A microfield approach. *Phys. Rev. E* **2016**, *94*, 012611.

(72) Hyun, J.-K.; Babu, C. S.; Ichiye, T. Apparent local dielectric response around ions in water: a method for its determination and its applications. *J. Phys. Chem.* **1995**, *99*, 5187–5195.

(73) Haggis, G.; Hasted, J.; Buchanan, T. The dielectric properties of water in solutions. *J. Chem. Phys.* **1952**, *20*, 1452–1465.

(74) Chandra, A. Static dielectric constant of aqueous electrolyte solutions: Is there any dynamic contribution? *J. Chem. Phys.* **2000**, *113*, 903–905.

(75) Friedman, H. Theory of the dielectric constant of solutions. *J. Chem. Phys.* **1982**, *76*, 1092–1105.

(76) Chan, D. Y.; Mitchell, D. J.; Ninham, B. W. A model of solvent structure around ions. *J. Chem. Phys.* **1979**, *70*, 2946–2957.

(77) Levy, A.; Andelman, D.; Orland, H. Dielectric constant of ionic solutions: A field-theory approach. *Phys. Rev. Lett.* **2012**, *108*, 227801.

(78) Allen, F.; Pon, A.; Greiner, R.; Wishart, D. Computational prediction of electron ionization mass spectra to assist in GC/MS compound identification. *Anal. Chem.* **2016**, *88*, 7689–7697.

(79) Hua, D.; Liu, X.; Go, E. P.; Wang, Y.; Hummon, A. B.; Desaire, H. How to Apply Supervised Machine Learning Tools to MS Imaging Files: Case Study with Cancer Spheroids Undergoing Treatment with the Monoclonal Antibody Cetuximab. *J. Am. Soc. Mass Spectrom.* **2020**, *31*, 1350–1357.

(80) Swan, A. L.; Mobasheri, A.; Allaway, D.; Liddell, S.; Bacardit, J. Application of machine learning to proteomics data: classification and biomarker identification in postgenomics biology. *OMICS* **2013**, *17*, 595–610.

(81) Verbeeck, N.; Caprioli, R. M.; Van de Plas, R. Unsupervised machine learning for exploratory data analysis in imaging mass spectrometry. *Mass Spectrom. Rev.* **2020**, *39*, 245–291.

(82) Liebal, U. W.; Phan, A. N.; Sudhakar, M.; Raman, K.; Blank, L. M. Machine learning applications for mass spectrometry-based metabolomics. *Metabolites* **2020**, *10*, 243.

(83) Wei, J. N.; Belanger, D.; Adams, R. P.; Sculley, D. Rapid prediction of electron–ionization mass spectrometry using neural networks. *ACS Cent. Sci.* **2019**, *5*, 700–708.